


Article

Design and CFD Analysis of the Energy Efficiency of a Point Wave Energy Converter Using Passive Morphing Blades

Changlei Wang, Zirong Luo , Zhongyue Lu ^{*}, Jianzhong Shang, Mangkuan Wang and Yiming Zhu

College of Intelligence Science and Technology, National University of Defense Technology, Changsha 410073, China

^{*} Correspondence: luozirong@nudt.edu.cn (Z.L.); luzhongyue03@163.com (Z.L.);

Tel.: +86-731-8457-4932 (Zirong Luo)

Abstract: A wave energy converter features the ability to convert wave energy into the electrical energy required by unmanned devices, and its energy-conversion efficiency is an essential aspect in practical applications. This paper proposes a novel point-absorption wave energy converter with passive morphing blades to meet the demand for improved energy-conversion efficiency. We first introduce its concept and design, with its blades forming their shape by adaptive changes with the direction of the water flow. Next, the three-dimensional geometrical-morphing model, energy-conversion model, and energy-conversion-efficiency model of the wave energy converter were established. Then, the CFD model was built to optimize the design parameters, and the simulation results revealed that the maximum conversion efficiency can be obtained at 90% solidity with 10 blades, a 40–60% load, and 20–25 degrees for the external deflection angle. The simulations also showed that the passive morphing-blade group provides ~40% higher torque and ~60% higher hydraulic efficiency than the flat-blade group.

Keywords: wave power; wave energy converter; power take-off; point absorption; passive morphing blade



Citation: Wang, C.; Luo, Z.; Lu, Z.; Shang, J.; Wang, M.; Zhu, Y. Design and CFD Analysis of the Energy Efficiency of a Point Wave Energy Converter Using Passive Morphing Blades. *Energies* **2023**, *16*, 204. <https://doi.org/10.3390/en16010204>

Academic Editor: Mário José Gonçalves Cavaco Mendes

Received: 8 November 2022

Revised: 18 December 2022

Accepted: 21 December 2022

Published: 25 December 2022



Copyright: © 2022 by the authors. Licensee MDPI, Basel, Switzerland. This article is an open access article distributed under the terms and conditions of the Creative Commons Attribution (CC BY) license (<https://creativecommons.org/licenses/by/4.0/>).

1. Introduction

Unmanned devices play an increasingly important role in ocean exploration and environmental protection. These facilities, such as detectors and marine buoys, mainly rely on batteries or cables for power supply, so an insufficient power supply has bottlenecked their durability and maneuverability performance. Thus, it is important to find new power supply methods that can recharge or power them [1–3]. Unmanned devices are surrounded by the ocean, which has various types of renewable ocean energy, such as wave energy, tidal energy, salt difference energy, wind energy, etc. [4]. It is a potential, economic, and feasible solution to convert these energies into electricity for the power supply of marine devices. Among these ocean energies, wave energy is a mechanical energy generated by the wind blowing along the ocean surface that is more easily harvested than other ocean energies [5,6]. Wave energy also has the characteristics of high energy density, wide distribution, and good predictability [7]. So it is feasible to use wave energy to power or recharge unmanned devices [8].

A wave energy converter (WEC) features the ability to convert wave energy into electrical energy. It typically consists of a wave-energy-capture module (a floating body on the water), an energy-converter module, an auxiliary module, etc. In addition, the energy converter module is the core working component, commonly referred to as a “power take-off (PTO)”. WECs have been developed for a long time: the first relevant patent was filed in France in 1799 by a father and son named Girard, and the amount of related research has increased significantly since 1980 [4]. However, there is no global consensus on the study of WECs [9], and most of these devices are large and built on the seacoast or inshore, where they are unsuitable for the power supply of unmanned devices directly.

To meet the power supply requirements of unmanned equipment, a compact, reliable, and efficient WEC is required; most importantly, it needs to be able to work safely in the deep sea without mooring. The point-absorption WEC can potentially achieve some of the above functions very well, such as high reliability, small size, a lack of mooring systems, etc. [8]. One extremely essential problem that needs to be focused on is how to improve its energy efficiency.

In recent years, a lot of research work has been done on point-absorption WEC [10], mostly on designing novel structures or optimizing the energy conversion process. IPS-buoy [11] consists of a buoy and an underwater pipe. When the buoy moves with the waves, it drives the piston in the pipe, which drives the hydraulic motor to generate electricity. As shown in Figure 1a PB3 PowerBuoy [12] consists of a water motion buoy and a submerged cylindrical device. When the buoy moves up and down with the waves, it will drive the hydraulic piston in the base to move and convert the wave energy into electricity through the rotary motor and generator. Wavebob [13] consists of two co-axial floating bodies, as shown in Figure 1b. The motion of the wave causes the two floating bodies to move relative to each other along the axial direction, driving the hydraulic system to convert the wave energy into mechanical energy and then into electrical energy. The AquaBuoy [14] uses its hose pump to feed water into an accumulator, then the water in the accumulator drives a water turbine (PTO) to generate electricity, as shown in Figure 1c. A common disadvantage of these devices is that their working stroke is limited by linear motors, hose pumps, or pistons, it is difficult to adapt to a wide range of waves in different sea conditions; in extreme environments, their PTOs may break through the working stroke's limits and cause damage to the device.

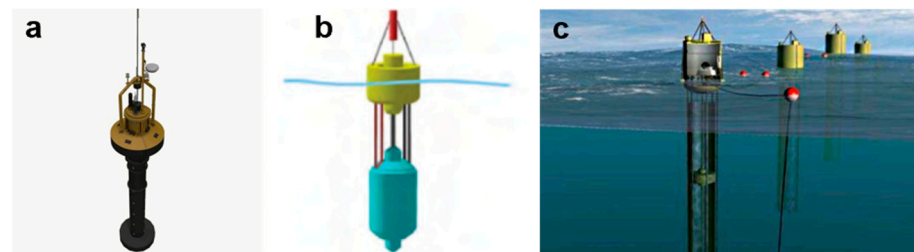


Figure 1. (a) PB3 PowerBuoy; (b) Wavebob; (c) AquaBuoy.

To address this problem, a small-size counter-rotating self-adaptable wave energy converter (CRWEC) was developed for unmanned marine equipment in a previous study by our group [15–17]. As shown in Figure 2a, our CRWEC consists of a PTO (energy-converter module), a floating body (wave-energy-capture module), and a counterweight (auxiliary module). The working principle of the PTO is shown in Figure 2b: it contains two counter-rotating blade groups. Under the action of the floating lift generated by the waves and the gravity of the counterweight, the rising and sinking motion generated by the PTO drives the two blade groups to rotate at a reverse differential speed, which drives the motor to generate electricity. In this design, the PTO uses flat blades to absorb energy, and the efficiency of the PTO is 26%. In a later, optimized design [15–17], flexible flat blades are used to improve efficiency to 37%. Even so, the efficiency of the blades still needs to be further improved by a new design.

Similar research on the wind turbine indicated that flat blades are not the best energy-harvesting blade type [18], as the twisted blades of the hydraulic turbine have better energy-absorption efficiency [19]. A recent study also indicated that a bird uses passive morphing wings to produce a higher lift [20]. Inspired by those designs, we propose a novel PTO with passive morphing-blade groups for a small point-absorption WEC. Compared to flat blades, the passive morphing blades have variable angles of attack to improve their energy-absorption efficiency. This is expected to solve the problem of low efficiency induced by flat blades.

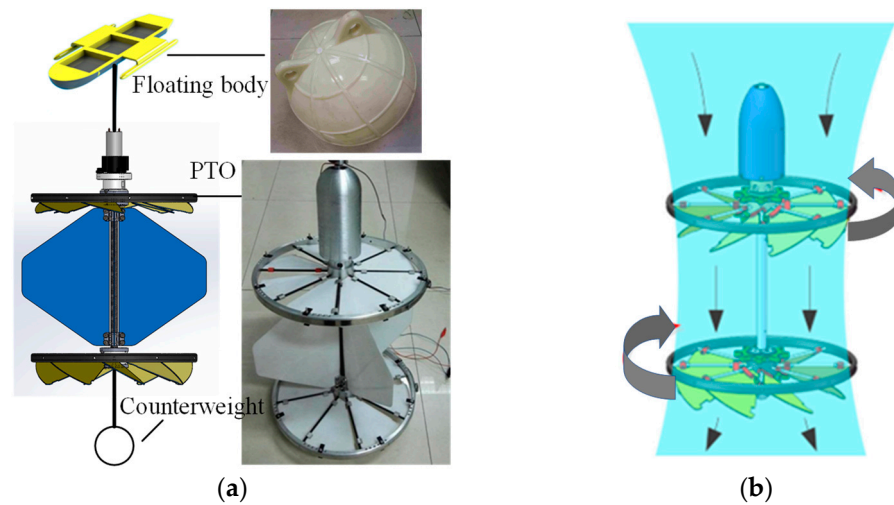


Figure 2. (a) Flat-blade PTO; (b) working principle.

The rest of the paper is structured as follows. Section 2 introduces the working principle and structure of the passive morphing blades in the PTO. Next, Section 3 proposes the energy-conversion process and energy-conversion-efficiency model for the PTO. Then, Section 4 analyzes the parameters that affect the PTO's operating performance, such as solidity, number of blades, the distance of the blade groups, and load, via FLUENT. The numerical-simulation results show that the energy-conversion efficiency and starting performance of the passive morphing-blade group are better than that of the flat-blade group. Finally, the paper ends with a conclusion in Section 5.

2. Working Principle and Structure

2.1. Working Principle of Point-Absorption WEC with Passive Morphing Blades

Ocean waves are surface waves, and research indicates that wave amplitudes are large at the ocean surface, though they decrease sharply with increasing water depth [21]. At a certain depth (≥ 10 m), seawater can be considered still water [22], providing a relative reference system for point-absorption WEC [23].

By adopting a similar principle and structure to the CRWEC and substituting the flat blades with morphing blades, we obtained a newly designed PTO. As shown in Figure 3a, the PTO consists of one float body 1 to capture wave motion, one drag rope, two counter-rotating morphing-blade groups 12 and 13, two generators 7, one drop rope 10, and one counterweight. In order to avoid the efficiency loss caused by mechanical transmission, we did not use the CRWEC's gear-differential transmission, so the blade group directly drives the motor to generate electricity.

As shown in Figure 3b, when the floating body 1 ascends with the wave, the PTO 14 ascends together under the traction of the drag rope 2, and the blade groups 12 and 13 of the PTO are deflected downward due to water resistance during the ascending process. At this time, the surface pressure difference of the up-blades will produce a right-handed force, driving the blade group 13 to rotate clockwise, while the down-blades produce a left-handed force and drive the blade group 12 to rotate counterclockwise. The counter-rotation of the two blade groups will automatically balance the torque and drive the generator to generate electricity.

Conversely, as shown in Figure 3c, when the floating body descends under the traction of counterweight 11, the blade groups will deflect upward. The surface pressure difference of the up-blades continues to produce a right-handed force, driving the blade group 13 to rotate clockwise, while the down-blades continue to produce a left-handed force, driving the blade group 12 to rotate counterclockwise. In this way, the passive morphing-blade group makes the PTO rotate in one direction, ensuring the continuity of the rotation process and avoiding the energy loss caused by the frequent reversal of the spindle.

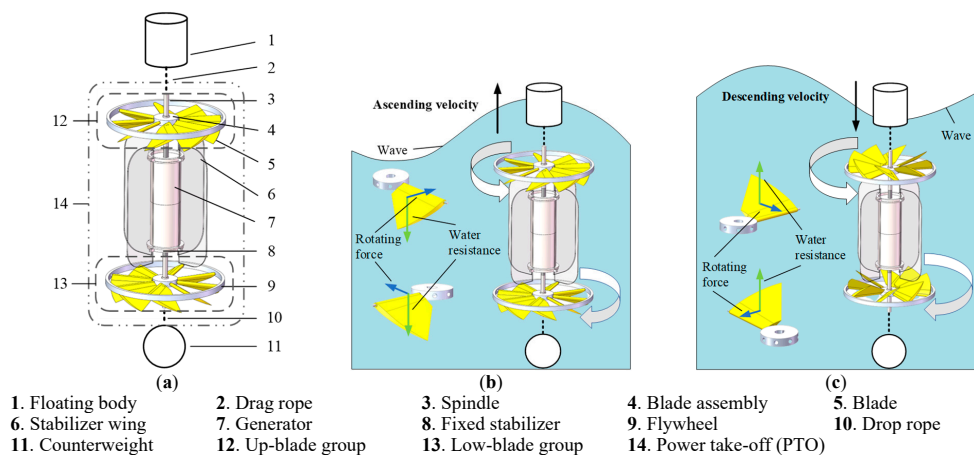


Figure 3. (a) Point-absorption WEC structure; (b) ascending process; (c) descending process.

2.2. Structure of Passive Morphing Blades

Twisted blades are widely used in rotating fluid machinery, especially wind turbine blades [24] and tidal-current turbine blades [1]. Since twisted blades can effectively reduce the axial drag coefficient of wind-turbine and tidal-energy-turbine-blade groups and improve the power and energy-conversion efficiency [25], this paper designed the passive morphing blade according to the twisted blade.

Unlike wind turbines and tidal turbines, which have blade groups that need to convert energy in only one direction, the PTO needs to absorb energy in two directions (the ascending and descending processes). To improve the energy-capture power and efficiency of CRWEC [15], this paper designed a passive morphing-blade group for the PTO based on a twisted blade, as shown in Figure 4. This has the advantages of both passive morphing blades and adaptive deflecting blades, ensuring the continuous unidirectional rotation of the blade groups and possessing a high energy-capture power and energy-conversion efficiency.

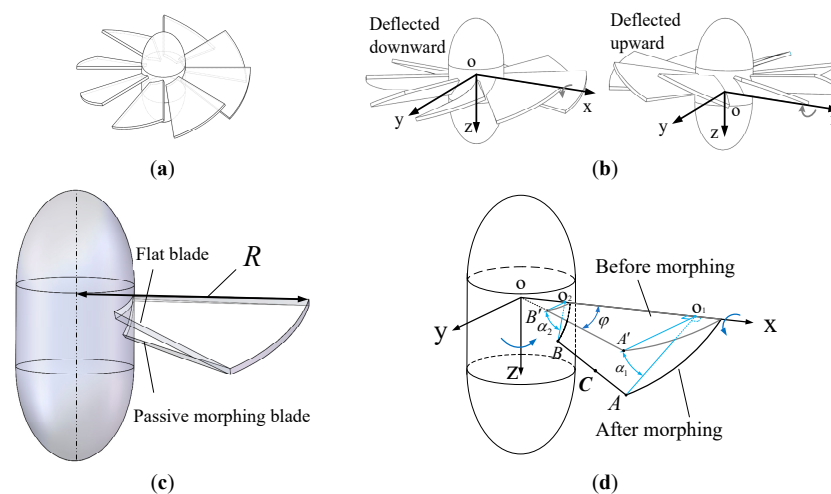


Figure 4. (a) Flat-blade group; (b) passive morphing-blade group; (c) difference between passive morphing blade and flat blade; (d) passive morphing-blade deflection principle.

The passive morphing blade, as shown in Figure 4a–c, is derived from the shape of the flat blade, with the exception being that the passive morphing blade has a greater internal deflection. As shown in Figure 4d, the passive morphing blade's deflection angle varies linearly along the X-axis. Before deflection, the two points, A' , B' on the passive morphing blade are in the rotation plane of the blade group. After deflection, the two points A , B on the passive morphing blade are deflected to their respective positions, and the deflection

angle of B is greater. The passive morphing blade is formed by extruding the surface F , which can be expressed as

$$\begin{cases} x = r \cos \varphi \\ y = r \sin \varphi \cos \alpha, \alpha = \arctan \frac{n}{m}, 0 \leq \varphi \leq \frac{2\pi\sigma}{Z}, R_{hub} \leq r \leq R \\ z = r \sin \varphi \sin \alpha \end{cases} \quad (1)$$

where m, n are the y, z coordinate values, respectively, of the point C in line AB , which can be expressed as

$$\frac{l - l_1}{l_2 - l_1} = \frac{m - m_1}{m_2 - m_1} = \frac{n - n_1}{n_2 - n_1} \quad (2)$$

where α' is the external deflection angle of the blade. The maximum internal declination angle is set to $\frac{\pi}{3}$.

$$\begin{aligned} A: (l_1, m_1, n_1) &= (R \cos \varphi, R \sin \varphi \cos \alpha', R \sin \varphi \sin \alpha') \\ B: (l_2, m_2, n_2) &= (R_{hub} \cos \varphi, R_{hub} \sin \varphi \cos \frac{\pi}{3}, R_{hub} \sin \varphi \sin \frac{\pi}{3}) \end{aligned}$$

To evaluate the performance of the PTO, we introduce two design parameters, T_{\max} and σ . The static torque T_{\max} is a parameter to measure the torque-output capacity of the blade group. It is defined as the maximum torque that the blade group can obtain under the impact of a fixed flow rate. The solidity σ is a dimensionless parameter that measures the geometric characteristics of the PTO blade groups. It is defined as the ratio of the total area of the blades to the area of the rotating plane.

$$\sigma = \frac{\sum_{i=1}^n S_{blade}}{\pi R^2} \quad (3)$$

where S_{blade} is the area of a single blade, and R is the blade's maximum radius.

3. Energy-Conversion-Efficiency Model of PTOs

3.1. Energy-Conversion Processes

As shown in Figure 5, the conversion from wave energy to electrical energy is an energy-decay process. First, the floating body captures the wave energy and converts it into the mechanical energy of its heave and roll motions (E_1); then, the floating body transfers the energy to the PTO through the drag rope and converts it into the mechanical energy of the PTO heave motion (E_2); the mechanical energy of its heave motion is converted into the mechanical energy of the spindle rotation (E_3); and, finally, the generator uses the rotational motion to generate electricity (E_4).

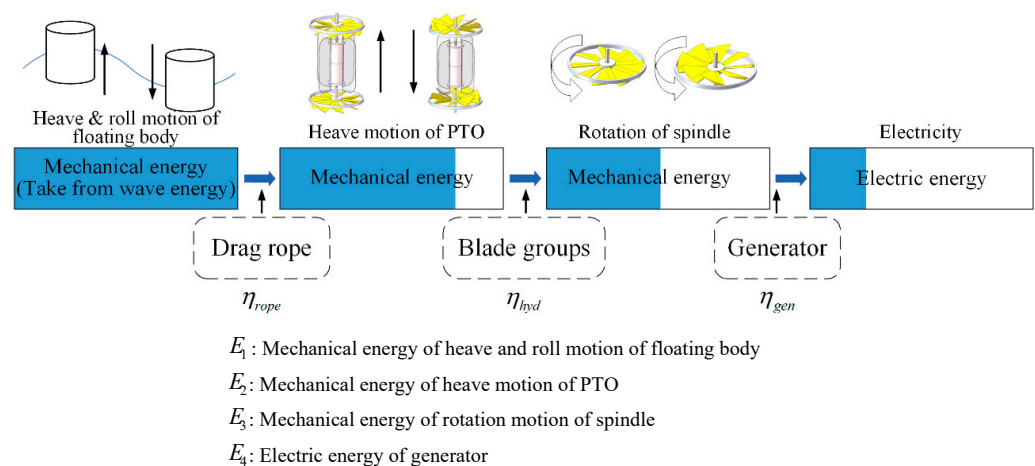


Figure 5. Energy-conversion processes of point-absorption WEC.

3.2. Energy-Conversion-Efficiency Evaluation Model

The energy-conversion efficiency η of the PTO mainly includes the hydraulic efficiency η_{hyd} of the blade groups and the power-generation efficiency η_{gen} of the generator. This can be expressed as

$$\eta = \eta_{hyd}\eta_{gen} \quad (4)$$

where $\eta_{hyd} = \frac{E_3}{E_2}$, $\eta_{gen} = \frac{E_4}{E_3}$.

Using the PTO as a reference system, the water flow impacts the PTO blade groups in an oscillating motion. The mechanical energy of the oscillating water flow is the only energy input of the PTO, and its power P_{input} is the kinetic energy flowing through the PTO per unit of time, which can be expressed as

$$P_{input} = \frac{E_k}{\Delta t} = \frac{\frac{1}{2}\rho(\pi R^2 \Delta h)v^2}{\Delta t} = \frac{1}{2}\pi\rho R^2 v^3 \quad (5)$$

The mechanical energy P_{output} of the spindle rotational motion is the output energy of the PTO blade group, which can be expressed as

$$P_{output} = \omega T = \frac{\pi n T}{30} \quad (6)$$

Equations (5) and (6) can be substituted into Equation (4):

$$\eta_{hyd} = \frac{P_{output}}{P_{input}} = \frac{\frac{\pi n T}{30}}{\frac{1}{2}\pi\rho R^2 v^3} = \frac{n T}{15\rho R^2 v^3} \quad (7)$$

Equation (7) can be used to calculate the PTO hydraulic efficiency η_{hyd} by using the rotational speed n , dynamic torque T , and flow rate v . Generator efficiency η_{gen} is load-dependent and will not be discussed in detail here.

4. CFD Numerical Simulation

4.1. CFD Modeling

The 6DOF function in FLUENT can simulate the passive motion of objects in the flow field. It can numerically simulate the static torque T_{max} , rotational speed n , and dynamic torque T of the PTO passive morphing-blade groups. However, the PTO performs a heave motion in still water, so it is more complicated to simulate it directly. To simplify the simulation process, the PTO is used as a reference system, and the water flow impinges on it with an oscillating motion [21]. To improve the accuracy of the numerical simulation, the passive morphing blades in the PTO are simplified to be fixed passive morphing blades, which helps to calculate the maximum power of the PTO. The instantaneous speed of the PTO heave motion is not constant and has some fluctuation. It has a draping speed range of 1–2.4 m/s in a class 2–4 sea state, so 1.5 m/s was chosen as the velocity inlet parameter for the numerical simulation.

Tetrahedral mesh is chosen for meshing because of its good adaptability to complex structures and flow fields. The multiple reference frame model (MRF) is used to simulate the passive rotation process of the blade groups inside the PTO. For the turbulence model, the RNG $k - \varepsilon$ model was chosen. It has a higher computational accuracy than the standard $k - \varepsilon$ model (since the rotation of objects and liquids is considered) and faster convergence than the realizable $k - \varepsilon$ model. By selecting “Velocity Inlet” as the inlet condition and “Pressure Outlet” as the outlet condition, the coupled methods help to simulate the coupling conditions in the real flow field. The rest of the parameters are mostly the defaults. More details about the six DOF parameters are shown in Table 1.

The sizes of the static and rotating grid areas have a great impact on the calculation time and accuracy. To save time and improve accuracy, some structures in the model are deleted or simplified, as shown in Figure 6a. After repeated modeling and calculations, the static grid area was set to be 1200 mm long, 1200 mm wide, and 4000 mm high; the rotating grid area was set to be 700 mm in diameter and 400 mm high; and the blade group was

set in the center of the rotating area. If the static and rotating grid areas are smaller than the above value, the calculation will not converge, which will lead to an inaccurate data calculation; the too large value will not improve the calculation accuracy but will greatly increase the calculation time. To observe the wake field conveniently, the rotating grid area is 350 mm away from the velocity inlet. As shown in Figure 6b, the grid size decreases when approaching the blade group to accurately simulate its motion. The static grid area is considered a stable flow field, while the rotating grid area is a flow field that directly impacts the blade group and is disturbed by the reaction.

Table 1. Six DOF parameters settings.

Options	Parameters
Mass	1 kg
Degree of freedom (DOF)	1 DOF rotation
Preload	$0.5 T_{\max}$
Moment of inertia	$0.5 \text{ kg}\cdot\text{m}^2$

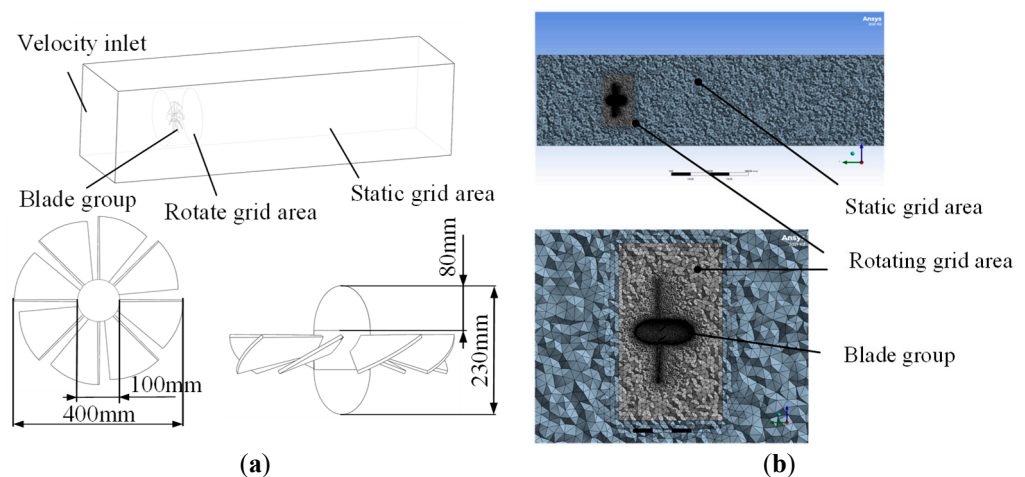


Figure 6. (a) Flow field model and simplified blade group model; (b) grid size comparison.

The grid number is equally important to the accuracy and convergence of the numerical-simulation results [26]. To verify the mesh independence, the twisted group with 10 blades with an external declination of 25 degrees was selected for analysis: the static torque simulation results T_{\max} will stabilize when the number of meshes is greater than 2.5 million. Similarly, in the transient simulation calculations, the timestep size and iteration number per timestep have a significant impact on the accuracy and total numerical-simulation time. Sun [15] found that choosing 20 iterations per timestep can save computational time while guaranteeing computational accuracy. Therefore, we studied the effect of timestep size on the simulation and found that if the timestep size is less than 0.01 s, the numerical simulation converges well and is repeatable, but when the timestep size is larger than 0.014 s, the result will become unstable or even scattered.

The numerical-simulation experiment consists of two parts. Firstly (static simulation), we calculated the T_{\max} of the fixed-blade group obtained from the impact of water flow; secondly (transient simulation), the blade group with a definite load ($0.5 T_{\max}$) was passively rotated under the push water flow to simulate the working performance of the PTO under loaded conditions. Doing the numerical simulation in the above order helps to improve the accuracy and shorten the convergence time. As a result, the transient simulation parameters are as follows: 1. iteration number: 20; 2. timestep value: 0.01 s; 3. transient simulation time size: 3.5 s.

4.2. Numerical-Simulation Result

4.2.1. Effect of the Passive Morphing Blades on the Hydraulic-Conversion Performance of PTO

Studies [15,25] found that the power and efficiency of the flat-blade group increased with the deflection angle and reached the maximum when the deflection angle was about 25 degrees, and then they decreased. The numerical simulation in this paper showed that the static torque T_{\max} and axial resistance of the passive morphing-blade group are larger than those of the flat-blade group (as shown in Figure 7a,b), which can provide greater rotational speed n and dynamic torque T (as shown in Figure 7c,d) and greatly improve the power P and hydraulic-conversion efficiency of the PTO (as shown in Figure 7e,f). Due to the energy-conversion-efficiency model (Equation (5)), the trends of power and hydraulic efficiency are consistent, and the hydraulic efficiency value is about half of the power, so the remaining part of our study mainly focuses on the power relationship.

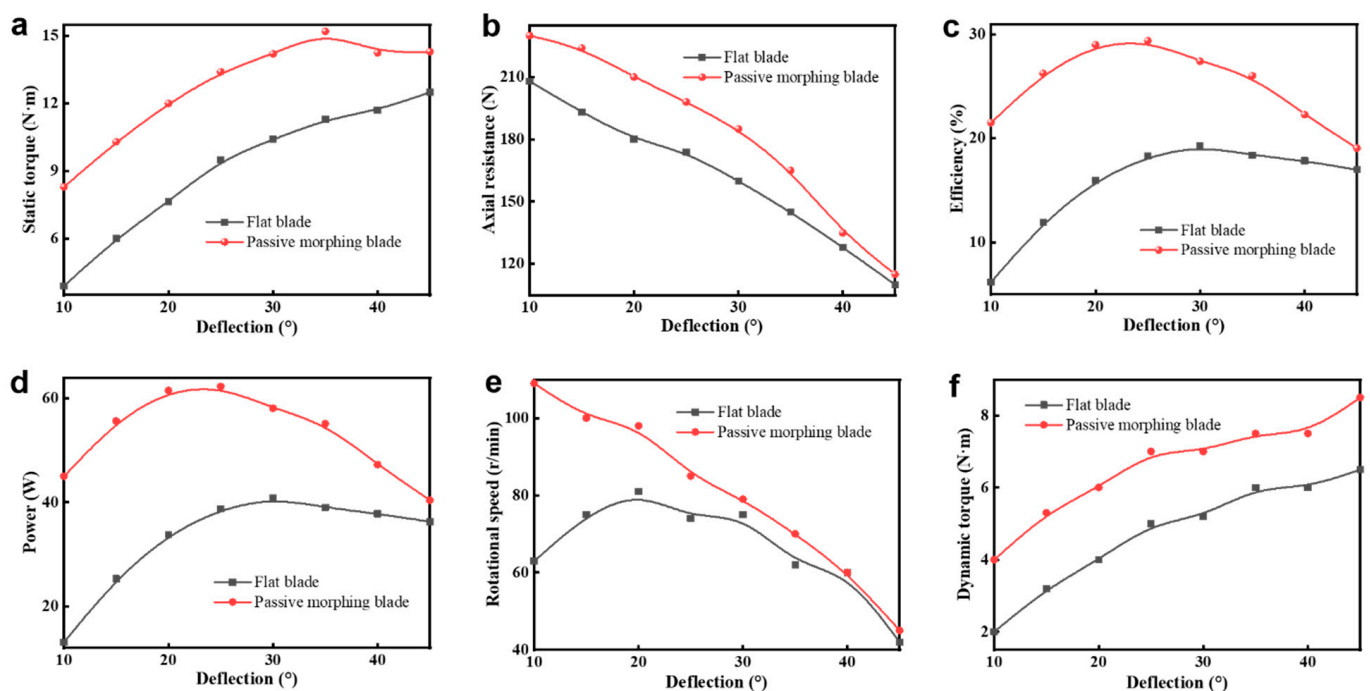


Figure 7. Effect of blades type and deflection angle on PTO: (a) static torque; (b) axial resistance; (c) efficiency; (d) dynamic torque; (e) power; (f) rotational speed.

The surface-pressure difference of the passive morphing-blade group is larger than that of the flat-blade group (as shown in Figure 8a,b), which may be caused by the higher rotational speed n of the passive morphing-blade group. Although the projected area of the passive morphing-blade group on the rotating plane is small, its twisted structure is beneficial to absorb the energy in the water flow, making it rotate faster. The numerical-simulation results show that the average static torque T_{\max} and dynamic torque T of the passive morphing blade group are 40% higher than those of the flat-blade group, and the average hydraulic-conversion efficiency η_{hyd} is 60% higher than that of the flat-blade group, so the passive morphing-blade group is more suitable for the PTO. Although the axial resistance of the passive morphing-blade group is larger (as shown in Figure 7b), the wave energy has a high energy density and a large lift, and the axial resistance is negligible.

The diameter of the twisted-blade group's wake field is 320 mm, which is smaller than the flat-blade group's (440 mm, as shown in Table 2 and Figure 8c–f). The passive morphing-blade group is more conducive to energy absorption, so the diameter of the vortex region is smaller, which is conducive to the smooth operation of the PTO.

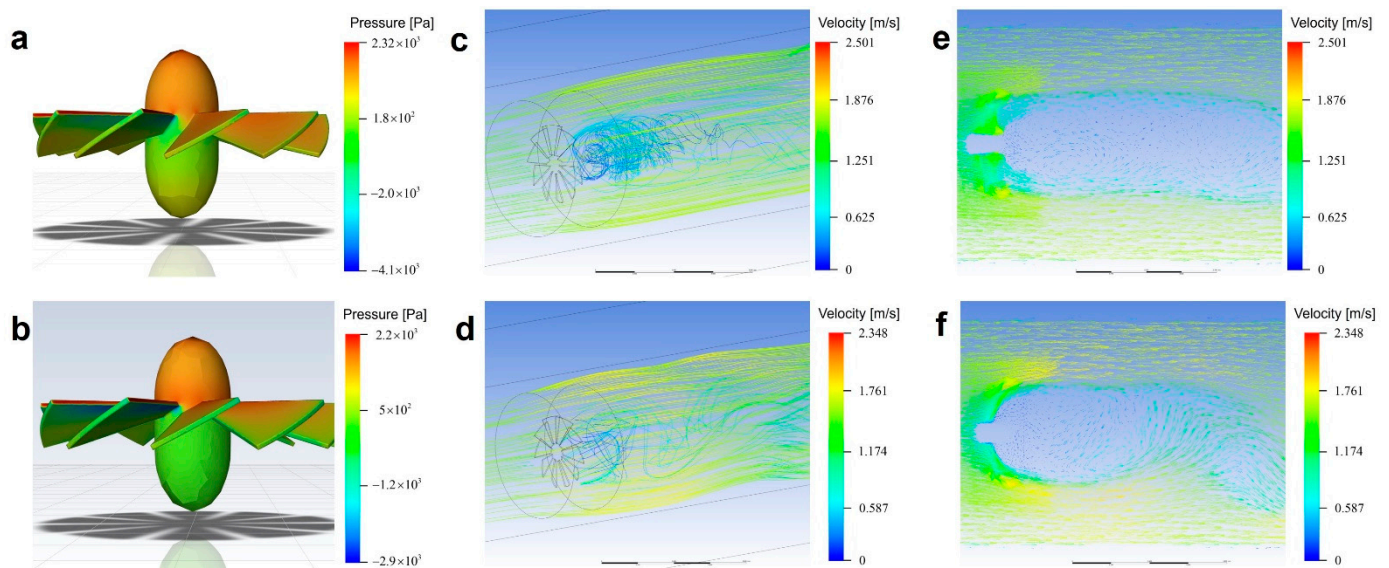


Figure 8. (a) Dynamic pressure distribution of passive morphing-blade group; (b) dynamic pressure distribution of flat-blade group; (c) path line around the tail of passive morphing-blade group; (d) path line around the tail of flat-blade group; (e) flow plane around the tail of passive morphing-blade group; (f) flow plane around the tail of flat-blade group.

Table 2. Parameters of wake field.

Blade Type	Wake Field Diameter	Wake Field Length
Passive morphing blades	320 mm	1500 mm
Flat blades	440 mm	900 mm

The numerical-simulation results show that the hydraulic performance of the passive morphing-blade group is better than the flat-blade group under various conditions, and the maximum power and efficiency can be obtained when the external deflection angle is 20° – 25° . Therefore, the passive morphing-blade group should be used in the PTO. The following numerical-simulation results are based on the passive morphing-blade group. In addition, the blade group's dynamic operating data (such as power, rotational speed, dynamic torque, etc.) are calculated under a 50% load condition and are not repeated below (except for special markings).

4.2.2. Effect of Blade-Group Solidity on the Hydraulic Performance of PTO

When the blade-group solidity is less than 70%, the static torque T_{\max} and power P of the PTO increase slowly, as shown in Figure 9a. However, when the blade-group solidity is between 70% and 90%, the static torque T_{\max} of the PTO increases rapidly. As shown in Figure 9b, a higher rotational speed n can be obtained when the blade-group solidity is 50–70%, but the output torque T and power P are low. The pressure (Figure 9c) follows a similar trend to the rotational speed (Figure 9e), and the relationship between the axial resistance (Figure 9c) and the dynamic torque (Figure 9e) is the same.

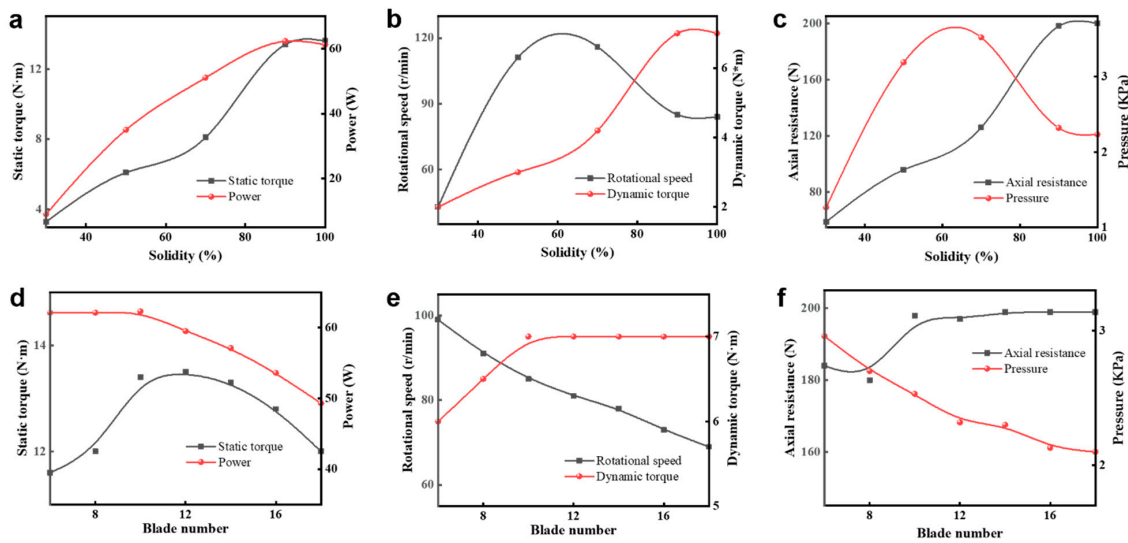


Figure 9. (a) Static torque and power relationship with solidity; (b) rotational speed and dynamic torque relationship with solidity; (c) axial resistance and dynamic pressure relationship with solidity; (d) static torque and power relationship with blade number; (e) rotational speed and dynamic torque relationship with blade number; (f) axial resistance and dynamic pressure relationship with blade number.

4.2.3. Effect of Blade Number on the Hydraulic Performance of PTO

Under the condition of fixed-blade-group solidity (90%) and flow rate (1.5 m/s), the static torque T_{\max} of the PTO shows a parabolic trend with the increase in the blade number, and a larger static torque is obtained when the number of blades is 10~14, as shown in Figure 9d. The output power P of the PTO decreases with the increase in the blade number, and a larger dynamic power is obtained when the blade number is 6~10. Therefore, 10 blades should be selected for PTO, which can obtain a greater dynamic power P and hydraulic-conversion efficiency η_{hyd} . As shown in Figure 9e, the rotational speed n gradually decreases with the increase in the blade number. Similar to Section 4.2.2, the pressure (Figure 9c) follows a similar trend to the rotational speed (Figure 9f), as does the axial resistance (Figure 9c) to the dynamic torque (Figure 9f).

4.2.4. Effect of the Blade Load Condition on the Hydraulic Performance of PTO

As shown in Figure 10a, the power P of the blade group increases with the load when the load is less than 60% and reaches a larger value at a 40~60% load. However, the power P and rotational speed n decrease sharply when the load exceeds 60%. Therefore, the blade group's load should be in the range of 40~60% of the static torque T_{\max} to obtain the maximum power P and hydraulic-conversion efficiency η_{hyd} . The pressure trend of on the blade is consistent with the speed, as shown in Figure 10b.

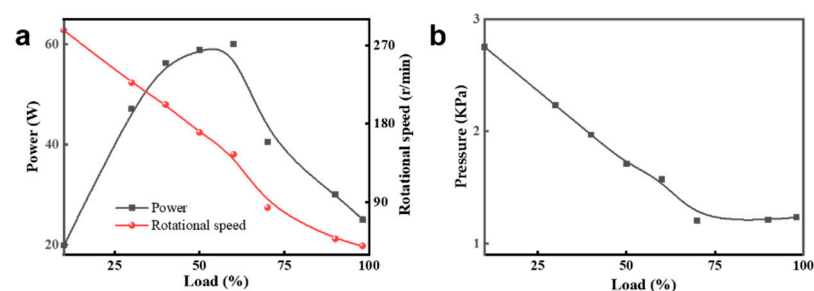
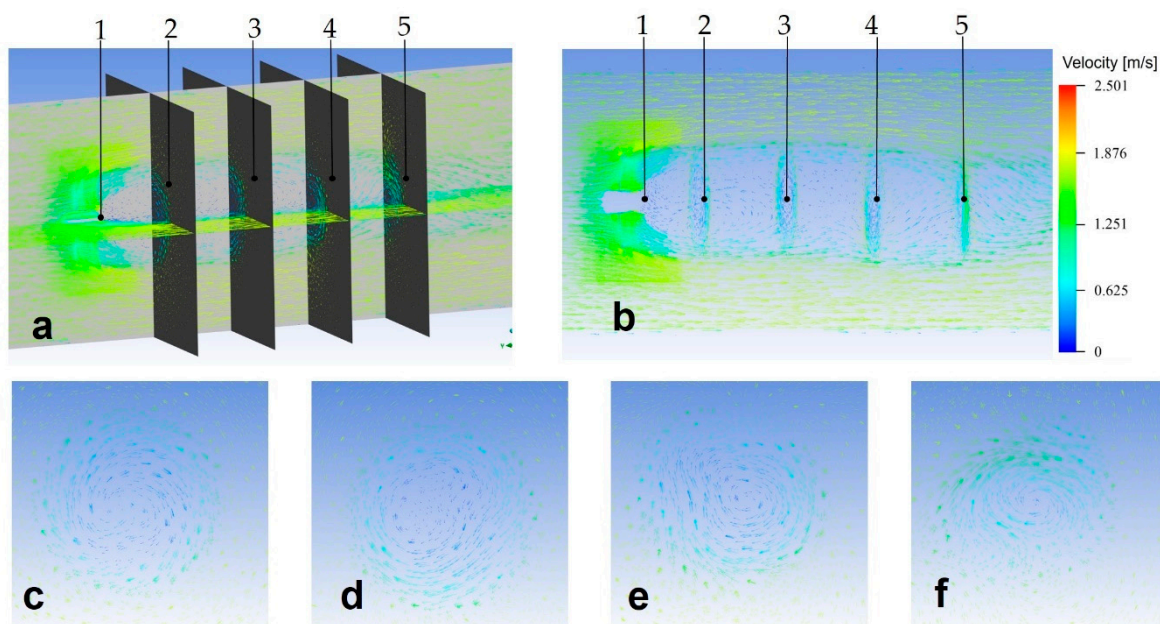


Figure 10. Effect of blade load on PTO under different load conditions: (a) rotational speed and power; (b) dynamic pressure.

The working principle of the blade group is the same as the resistance fan because the high-solidity blade group is a blunt body that hinders the flow, and the theoretical maximum energy-conversion efficiency of the resistance fan is 59.3% (Bates' law). The water flow impacts the blades: part of it flows directly from the blades' gap, and the other part of the fluid pushes the blades to rotate and move to the outside of the blades, as shown in Figure 8e, which is one of the most important reasons for the low hydraulic efficiency of the PTO. As shown in Figure 8c,e, the water flow is blocked by the blade group and flows to the outside of it. An obvious low-pressure vacuum belt is formed at the rear of the blade group, resulting in a back-flow around it. Due to the low-pressure vacuum belt, bubbles and eddy currents are formed in this position, and the other blade group should be arranged away from this position. In addition to the back-flow, there are obvious vortices at the tail of the flow field (opposite to the direction of the blade group's rotation), which is caused by the reverse motion of the water flow, as shown in Figure 11a,b.



1. Blade group
2. The cross-section at 1 time the of from the blade
3. The cross-section at 2 times the diameter of the blade
4. The cross-section at 3 times the diameter of the blade
5. The cross-section at 4 times the diameter of the blade

Figure 11. Wake field vector of the passive morphing blade: (a) section in the wake field; (b) wake field vector; (c) vector in cross—Section 2; (d) vector in cross—Section 3; (e) vector in cross—Section 4; (f) vector in cross—Section 5.

As shown in Figure 11c–f, the back-flow and reverse vortex are unavoidable, but they always occur within a distance of four times the blade diameter; the reverse vortex in the cross section at four times the blade diameter is largely invisible, as shown in Figure 11f. Therefore, the two blade groups' distances should be greater than four times the diameter of the blade group. The reverse vortex field length is close to the back-flow field, and a spoiler should be installed inside the PTO to reduce the influence of the reverse vortex on the other group of blades [7].

Figure 12a–c show the wake field of the 6-blade group, 10-blade group, and 16-blade group, and their shapes are basically similar, which shows that the wake field is not affected

by the number of blades. To verify the accuracy of the simulation results of the wake field, the motion process of the blade group in the static water flow is numerically simulated. Figure 12d–i show the wake field when the passive morphing-blade group moves to 0.3 s, 0.9 s, 1.3 s, 1.4 s, 1.5 s, and 1.6 s, respectively. The strong disturbance influence on the flow field tended to be stable after the blade moved in the static flow field for 1.3 s. It can be seen that the numerical-simulation results are the same, which proves the accuracy of these results.

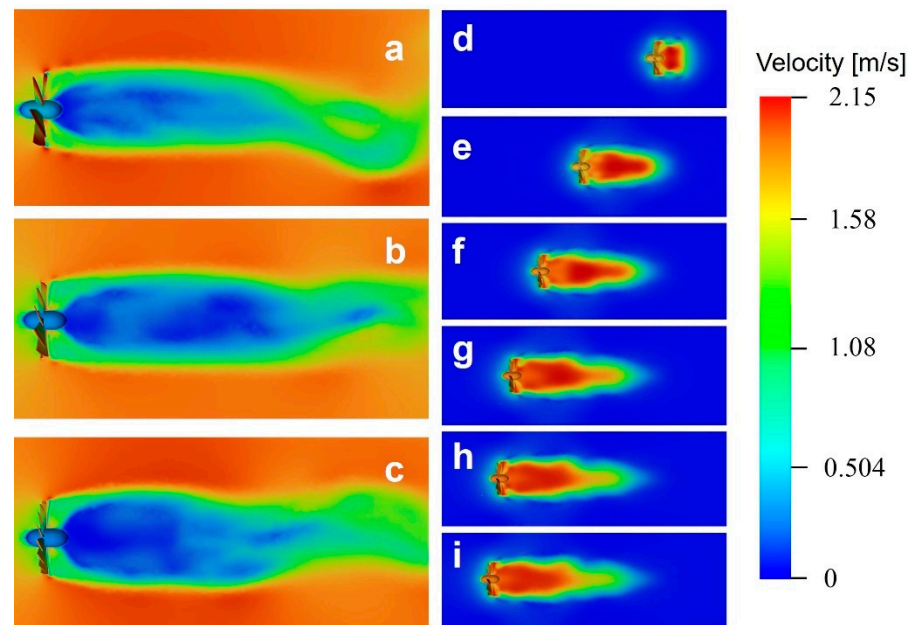


Figure 12. (a) Wake field of 6-blade group; (b) wake field of 10-blade group; (c) wake field of 16-blade group; (d) wake field when the blade group moves to 0.3 s; (e) wake field when the blade group moves to 0.9 s; (f) wake field when the blade group moves to 1.3 s; (g) wake field when the blade group moves to 1.4 s; (h) wake field when the blade group moves to 1.5 s; (i) wake field when the blade group moves to 1.6 s.

5. Conclusions

In this paper, we proposed a novel PTO with passive morphing-blade groups that can efficiently convert wave energy into electricity. Its properties were investigated through modeling, design, and numerical simulation. It was found that the energy absorption properties of passive morphing-blade groups are better than those of flat-blade groups. The relevant parameters affecting the static torque T_{\max} , power P , and hydraulic conversion efficiency η_{hyd} were also analyzed via numerical simulation (e.g., external deflection angle, blade number, solidity, load, flow rate, etc.). The detailed findings are summarized as follows.

1. The dynamic torque T , power P , and hydraulic conversion efficiency η_{hyd} of the PTO increase with the blade group's solidity, with a fixed blade number, deflection angle, and load ratio. The maximum energy-conversion efficiency is achieved when the blade group solidity is about 90%.
2. A 10-blade group, with a fixed-blade-group solidity (90%), deflection angle (20°), and load ratio (50%), has a large dynamic torque and a large power, and is suitable as a reference value for the number of blades of a PTO.
3. The passive morphing-blade group produces a smaller wake-field diameter, when the other conditions are identical. The passive morphing-blade group provides ~40% higher torque T and ~60% higher hydraulic efficiency η_{hyd} than the flat-blade group.
4. For PTOs with two blade groups, the wake field has a great effect on the rotational speed n , torque T , power P , and hydraulic-conversion efficiency η_{hyd} . The distance

between the two passive morphing-blade groups should be spaced four times larger than the blade diameter to reduce the intergroup wake-field effects.

Author Contributions: Conceptualization, C.W. and Z.L. (Zirong Luo); software, C.W. and M.W.; data curation, C.W.; writing—original draft preparation, C.W. and Z.L. (Zhongyue Lu); writing—review and editing, Y.Z., Z.L. (Zirong Luo) and J.S. All authors have read and agreed to the published version of the manuscript.

Funding: This research was funded by the National Natural Science Foundation of China, grant number 52075537.

Data Availability Statement: The data used to support the findings of this study are available from the corresponding author upon request.

Conflicts of Interest: The authors declare no conflict of interest.

Nomenclature

The following abbreviations are used in this manuscript:

α'	outermost deflection angle of blade
α_1	deflection angle of $\angle Ao_1A'$
α_2	deflection angle of $\angle Bo_1B'$
η_{hyd}	hydraulic efficiency
η_{gen}	generation efficiency
ρ	density, $\text{kg}\cdot\text{m}\cdot\text{s}^{-2}$
σ	ratio of blade area to blade rotating flat area
ω	angular velocity, rad/s
E_1	mechanical energy of floating body's heaving and pitching motion, W
E_2	mechanical energy of PTO's dipping motion, W
E_3	mechanical energy of transmission shaft, W
E_4	electric energy, W
n	rotation speed, r/s
P	dynamic power, W
P_{input}	input power, W
P_{output}	output power, W
R	maximum radius of blade, mm
R_{hub}	hub radius, mm
r	blade radius, mm
S_{blade}	blade area, mm^2
T	dynamic torque, $\text{N}\cdot\text{m}$
T_{max}	maximum torque of blade under impact of steady flow field, $\text{N}\cdot\text{m}$
Δt	unit time, s
v	flow rate, m/s

References

1. López, I.; Andreu, J.; Ceballos, S.; Martínez de Alegría, I.; Kortabarria, I. Review of wave energy technologies and the necessary power-equipment. *Renew. Sustain. Energy Rev.* **2013**, *27*, 413–434. [\[CrossRef\]](#)
2. Tiron, R.; Mallon, F.; Dias, F.; Reynaud, E.G. The challenging life of wave energy devices at sea: A few points to consider. *Renew. Sustain. Energy Rev.* **2015**, *43*, 1263–1272. [\[CrossRef\]](#)
3. Li, Y.; Yu, Y.-H. A synthesis of numerical methods for modeling wave energy converter-point absorbers. *Renew. Sustain. Energy Rev.* **2012**, *16*, 4352–4364. [\[CrossRef\]](#)
4. Falcão, A.F.d.O. Wave energy utilization: A review of the technologies. *Renew. Sustain. Energy Rev.* **2010**, *14*, 899–918. [\[CrossRef\]](#)
5. Dai, Y.; Chen, Y.; Xie, L. A study on a novel two-body floating wave energy converter. *Ocean Eng.* **2017**, *130*, 407–416. [\[CrossRef\]](#)
6. Amiri, A.; Panahi, R.; Radfar, S. Parametric study of two-body floating-point wave absorber. *J. Mar. Sci. Appl.* **2016**, *15*, 41–49. [\[CrossRef\]](#)
7. Yu, Y.-H.; Li, Y. Reynolds-Averaged Navier–Stokes simulation of the heave performance of a two-body floating-point absorber wave energy system. *Comput. Fluids* **2013**, *73*, 104–114. [\[CrossRef\]](#)
8. Sun, C.; Luo, Z.; Zhu, Y.; Lu, Z.; Wu, G.; Shang, J. Structural Design and Numerical Optimization of Novel Wave Energy Point Absorber. *Energies* **2018**, *49*, 406–413. [\[CrossRef\]](#)

9. Son, D.; Belissen, V.; Yeung, R.W. Performance validation and optimization of a dual coaxial-cylinder ocean-wave energy extractor. *Renew. Energy* **2016**, *92*, 192–201. [[CrossRef](#)]
10. Zhang, Y.X.; Zhao, Y.J.; Sun, W.; Li, J.X. Ocean wave energy converters: Technical principle, device realization, and performance evaluation. *Renew. Sustain. Energy Rev.* **2021**, *141*, 110764–110784. [[CrossRef](#)]
11. Falcão, A.F.O.; Cândido, J.J.; Justino, P.A.P.; Henriques, J.C.C. Hydrodynamics of the IPS buoy wave energy converter including the effect of non-uniform acceleration tube cross section. *Renew. Energy* **2012**, *41*, 105–114. [[CrossRef](#)]
12. Rezaei, S.; Rahimi, A.; Parvizian, J.; Mansourzadeh, S.; Düster, A. Dimensional optimization of a two-body Wave energy converter using response surface methodology. *Ocean Eng.* **2022**, *261*, 112186. [[CrossRef](#)]
13. Abdelkhalik, O.; Zou, S. Control of small two-body heaving wave energy converters for ocean measurement applications. *Renew. Energy* **2019**, *132*, 587–595. [[CrossRef](#)]
14. Weinstein, A.; Fredrikson, G.; Parks, M.J.; Nielsen, K. Numerical evaluation of a two-body point absorber wave energy converter with a tuned inerter. *Renew. Energy* **2021**, *171*, 217–226.
15. Sun, C.; Luo, Z.; Shang, J.; Lu, Z.; Zhu, Y.; Wu, G. Design and Numerical Analysis of a Novel Counter-Rotating Self-Adaptable Wave Energy Converter Based on CFD Technology. *Energies* **2018**, *11*, 694. [[CrossRef](#)]
16. Sun, C.; Shang, J.; Luo, Z.; Zhu, Y.; Lu, Z.; Wu, G.; Cong, D. Performance characteristics of a Novel point Absorber-type WEC based on counter-rotating self-adaptable movement mechanism. *Energy Sources Part A Recovery Util. Environ. Eff.* **2021**, *43*, 783–799. [[CrossRef](#)]
17. Sun, C.; Shang, J.; Luo, Z.; Lu, Z.; Wu, G.; Zhu, Y. Using Flexible Blades to Improve the Performance of Novel Small-Scale Counter-Rotating Self-Adaptable Wave Energy Converter for Unmanned Marine Equipment. *J. Mar. Sci. Eng.* **2019**, *7*, 223. [[CrossRef](#)]
18. Johansen, J.; Sorensen, N.N. Aerofoil characteristics from 3D CFD rotor computations. *Wind Energy* **2004**, *7*, 283–294. [[CrossRef](#)]
19. Setoguchi, T.; Santhakumar, S.; Maeda, H.; Takao, M.; Kaneko, K. A review of impulse turbines for wave energy conversion. *Renew. Energy* **2001**, *23*, 261–292. [[CrossRef](#)]
20. Matloff, L.Y.; Chang, E.; Feo, T.J.; Jeffries, L.; Stowers, A.K.; Thomson, C.; Lentink, D. How flight feathers stick together to form a continuous morphing wing. *Science* **2020**, *367*, 293–297. [[CrossRef](#)]
21. Goteman, M. Wave energy parks with point-absorbers of different dimensions. *J. Fluids Struct.* **2017**, *74*, 142–157. [[CrossRef](#)]
22. Dafnakis, P.; Bhalla, A.P.S.; Sirigu, S.A.; Bonfanti, M.; Bracco, G.; Mattiazzo, G. Comparison of wave-structure interaction dynamics of a submerged cylindrical point absorber with three degrees of freedom using potential flow and computational fluid dynamics models. *Phys. Fluids* **2020**, *32*, 1–20. [[CrossRef](#)]
23. Xudong, W.; Shen, W.Z.; Zhu, W.J.; Sorensen, J.N.; Jin, C. Shape Optimization of Wind Turbine Blades. *WIND ENERGY* **2009**, *12*, 781–803. [[CrossRef](#)]
24. Ye, X.M.; Fan, F.W.; Zhang, R.X.; Li, C.X. Prediction of Performance of a Variable-Pitch Axial Fan with Forward-Skewed Blades. *ENERGIES* **2019**, *12*, 2353. [[CrossRef](#)]
25. Al Shami, E.; Wang, X.; Zhang, R.; Zuo, L. A parameter study and optimization of two body wave energy converters. *Renew. Energy* **2019**, *131*, 1–13. [[CrossRef](#)]
26. Poguluri, S.K.; Ko, H.S.; Bae, Y.H. CFD investigation of pitch-type wave energy converter-rotor based on RANS simulations. *Ships Offshore Struct.* **2020**, *15*, 1107–1119. [[CrossRef](#)]

Disclaimer/Publisher’s Note: The statements, opinions and data contained in all publications are solely those of the individual author(s) and contributor(s) and not of MDPI and/or the editor(s). MDPI and/or the editor(s) disclaim responsibility for any injury to people or property resulting from any ideas, methods, instructions or products referred to in the content.